Supplemental Materials–Small-scale intermittency of premixed turbulent flames

Amitesh Roy[1]†‡, Jason R. Picardo[2]¶, Benjamin Emerson[3], Tim C. Lieuwen[3] and R. I. Sujith[1]

[1]Department of Aerospace Engineering, IIT Madras, Chennai 600 036, India

[2]Department of Chemical Engineering, IIT Bombay, Mumbai 400 076, India

[3]Daniel Guggenheim School of Aerospace Engineering, Georgia Institute of Technology, Atlanta, Georgia, 30332, USA

(Received 19 March 2022; revised 15 November 2022; accepted 17 January 2023)

S1. Experiments, instrumentation and diagnostics

S1.1. *Setup*

The turbulent combustor used in our study of small-scale intermittency is shown in figure S1. This experimental configuration was designed to assess how flame dynamics are affected by broadband forcing due to turbulence in addition to narrowband forcing due to an oscillating flame-holder (Petersen & Emmons 1961; Kornilov *et al.* 2007; Truffaut & Searby 1999).

Air and methane (CH_4) enter the premixing chamber through a port at the bottom. The premixing chamber is packed with ball bearings to facilitate thorough mixing of the fuel and air. Next, the mixture of air and CH_4 enters the settling chamber and then passes through the turbulence generator and onward to the combustion chamber through a nozzle. The entry into the combustion chamber is aided by a co-flow of air, injected through the co-flow air channel at the bottom of the nozzle. The main nozzle has an exit diameter of 27.4 mm. The co-flow is velocity matched to the main flow and ensues out of an annulus with an outer diameter of 36.3 mm. The main air and fuel flow supply are controlled using Aalborg GFC-67, 0 – 500 L/min and Omega FMA-5428, 0 – 50 L/min mass flow controllers, respectively. The co-flow is controlled using an Omega FMA-1843 gas flow meter and needle valve. All the mass flow controllers have an uncertainty of ±1%. The maximum uncertainty in the reported values of equivalence ratio (ϕ), velocity ($\boldsymbol{u}$) and Reynolds number (Re) are ±2%, ±1% and ±1%, respectively.

An electrically heated flame holder ignites the flame. The flame holder is a nichrome wire (0.81 mm, 20 American Wire Gauge) and is heated by 6 – 12 V alternating current and held 10 mm above the exit plane of the main nozzle. The flame holder is oscillated, transverse to the oncoming jet flow, at different frequencies and with different forcing amplitudes, using two modified 90 W Goldwood speakers connected in parallel. The input signal to the speakers is generated using a function generator and amplified by two linear amplifiers. Experiments

† Email address for correspondence: amiteshroy94@yahoo.in
‡ Presently at Institute for Aerospace Studies, University of Toronto, Ontario M3H 5T6, Canada
¶ Also, Associate, International Centre for Theoretical Sciences, TIFR, India.

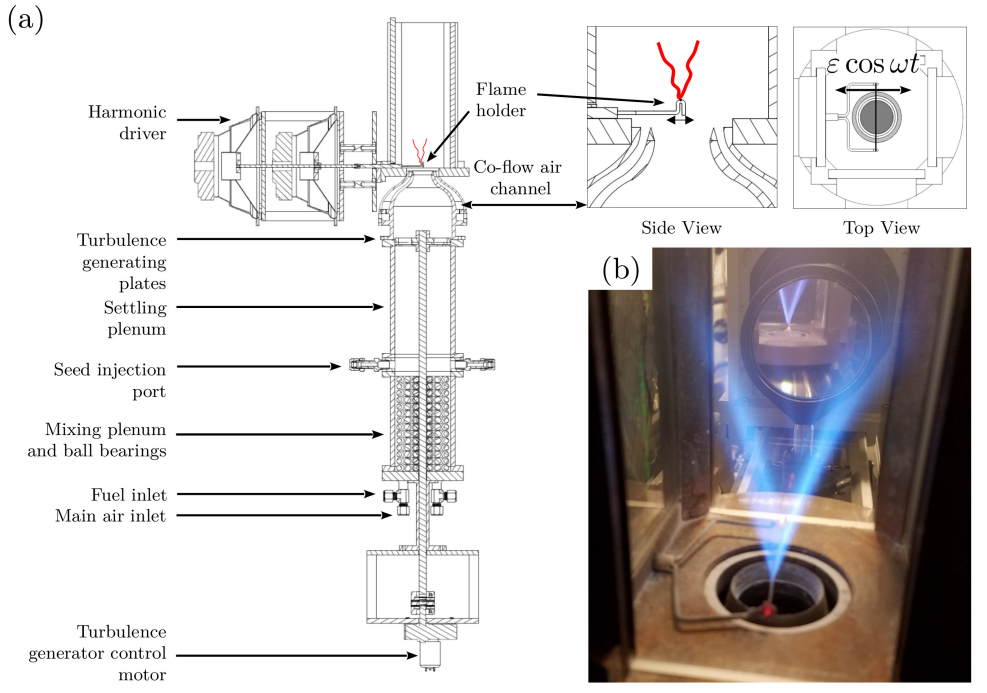

Figure S1: Turbulent V-flame facility. (a) Schematic of the combustor setup. (b) Illustrative photograph of the V-flame. Adapted from (Humphrey *et al.* 2018) with permission from Cambridge University Press.

reported in this paper were conducted for a forcing frequency of $f_f = 1250$ Hz and amplitude of $\langle \varepsilon(f_f) \rangle \approx 0.26$ mm. The amplitude of forcing is determined from the power spectrum of the measured time series of the position of the flame holder.

The turbulence generator consists of two plates with several pie-shaped slots cut through them. The bottom plate is fixed (stator), and the top plate (rotor) can be rotated over a $28 \pm 0.25^\circ$ range. By rotating the rotor, it is possible to change the blockage ratio from 69% to 97%, which in turn enables us to vary the turbulent intensity, $u'/\bar{u}_y$, in the range of 8% to 36%. Under isothermal conditions, the turbulent flow so generated exhibits a Kolmogorov energy spectrum (Marshall *et al.* 2011).

S1.2. *Optical Diagnostic*

The optical diagnostic setup used for simultaneously measuring the flame dynamics and the turbulent flow is shown in figure S2. The flame edge is detected using TiO_2 Mie scattering, and the velocity field is quantified through particle image velocimetry (PIV). Flame images are acquired using Photron Fastcam SAS high-speed video camera with a Nikon Micro-Nikkor $f = 55$m $f/2.8$ lens. For the experiments, the resolution was set at 640×848 pixels. The camera and laser pulse are controlled together by a dual head and are triggered together by a timing box. The laser used for diagnostics is a frequency-doubled Litron Nd:YLF with 527 nm wavelength. The sampling frequency of Mie scattering imaging was kept fixed at $f_s = 1.25 \times 10^4$ Hz to eliminate spectral leakage and bias errors in spectral estimation. In total, 21094 images were obtained for 1.68 s for each of the two flame configurations considered here.

The flow is seeded with Titanium dioxide (TiO_2) particles having a nominal diameter of 1 μm. The seeding is achieved by a cyclone seeder through which a portion of the main air

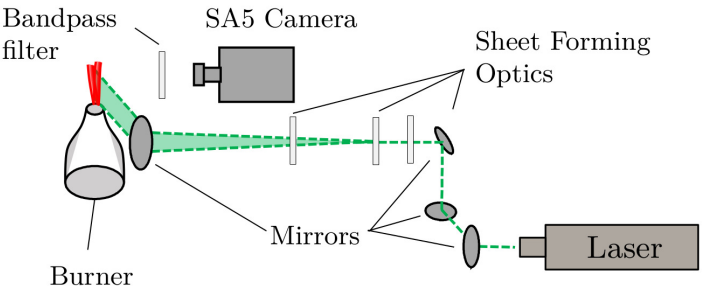

Figure S2: Arrangement of the optical diagnostic setup for measuring the flame surface and velocity field. Adapted from Humphrey *et al.* (2018) with permission from Cambridge University Press.

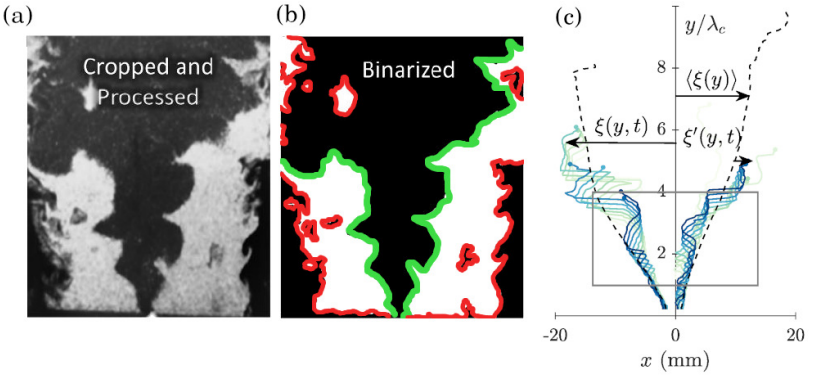

Figure S3: (a) Cropped and processed Mie scattering image of the flame. (b) Binarized flame image following Otsu's method (Otsu 1979). (c) Single-valued instantaneous $\xi(y,t)$, mean $\langle\xi(y)\rangle$ and fluctuating $\xi'(y,t)$ flame surface. The flame edges here represent the leading edge, which is described in the text. Panel a,b have been adapted from (Humphrey *et al.* 2018) with permission from Cambridge University Press.

is diverted before the premixing plenum. The seeded flow enters upstream of the settling chamber, as can be seen in figure S1. Only the main flow is seeded.

LaVision DaV PIV software (LaVision 2006) is used to process the PIV using a multipass algorithm. The first pass of which uses a 48×48 pixel interrogation window with a 25% overlap between windows. The subsequent passes use an 8×8 pixel window, with 25% overlap. This results in a resolution of 6 pixels ($\sim$ 0.46 mm) between vectors. For a description of uncertainty in PIV measurements, kindly refer to (Humphrey *et al.* 2018; Humphrey 2017).

S2. Flame edge detection

Raw images acquired during the experiments are de-wrapped using LaVision DaVis PIV processing software to remove flame distortions due to the presence of the glass window. Figure S3(a) shows a representative flame image that has been cropped and processed. The Mie scattering images are then binarized using a weighted threshold based on Otsu's method (Otsu 1979). Figure S3(b) shows the resultant binarized image. The identified flame front from the binarized edge is indicated in green in figure S3(b). As the flame-flow interaction lies in the limit of corrugated flamelets and thin reaction zone (cf. figure S4), the flame front remains continuous (Chowdhury & Cetegen 2017), allowing for a well-defined description of the flame front. We extract the instantaneous flame edge $\widetilde{\xi}(x,y,t)$, while ignoring any flame

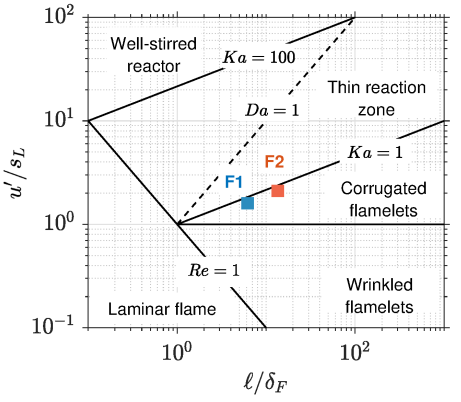

Figure S4: Turbulent premixed flame regime diagram indicating the properties of Flame F1 and F2 considered in the present study.

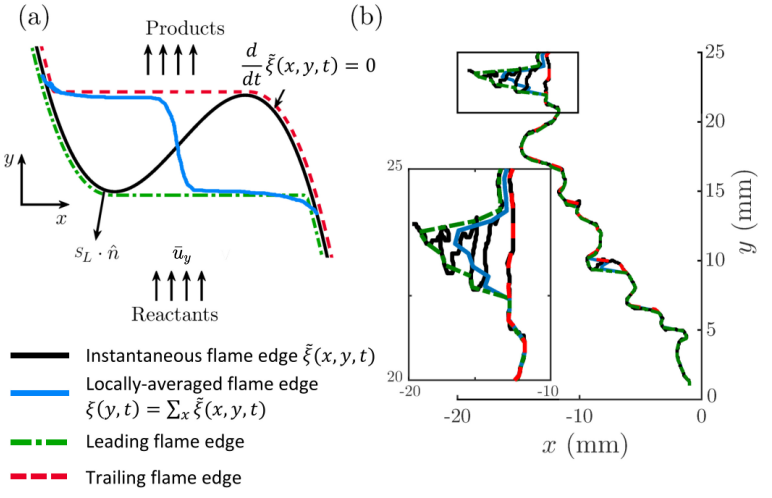

Figure S5: (a) Exaggerated pictorial depiction of converting multi-valued flame front $\widetilde{\xi}(x,y,t)$ into a locally averaged, leading and trailing flame edge $\xi(y,t)$. These single-valued flame edges are shown for a representative flame edge in (b).

holes or islands that may be present. The mean and instantaneous flame edges are shown in figure S3(c), where x indicates the spanwise and y indicates the streamwise direction.

Here, $\widetilde{\xi}(x,y,t)$ can be multivalued, i.e., for a given axial location there are multiple flame positions. We extract a single-valued flame position, $\xi(y,t)$ by three different strategies to obtain (i) a locally-averaged flame edge, (ii) a leading flame edge and (iii) a trailing flame edge, as follows:

(i) We first calculate the time-averaged flame position:

$$\langle \xi(y) \rangle = \frac{1}{N_t} \sum_t \frac{1}{N_x(t)} \sum_{x(t)} \widetilde{\xi}(x,y,t), \tag{S2.1}$$

where N_t refers to the number of images in the time series, and N_x refers to the number of multi-valued flame locations in the x direction for a given y location at a given instant of time. Thus, if the flame is not multi-valued at a given time instant, $N_x = 1$.

(ii) We define the instantaneous, *locally averaged* flame edge, by averaging over all the x-locations at which the flame is multi-valued, as

$$\xi(y,t) = \frac{1}{N_x}\sum_x \{\widetilde{\xi}(x,y,t)\}. \tag{S2.2}$$

(iii) We define the *leading* and *trailing* flame edges as

$$\xi(y,t) = \begin{cases} \sup\{\widetilde{\xi}(x,y,t)\}, & \text{Leading Edge} \\ \\ \inf\{\widetilde{\xi}(x,y,t)\}, & \text{Trailing Edge} \end{cases} \tag{S2.3}$$

here, sup and inf are the *supremum* and *infimum* of the set $\{\widetilde{\xi}(x,y,t)\}$. Thus, the leading and trailing flame edge are the farthest and closest points on the flame front from the y-axis at every streamwise location, respectively, while the locally averaged flame edge resides at an intermediate position between these extremes.

(iv) Finally, the fluctuations are determined as $\xi'(y,t) = \xi(y,t) - \langle\xi(y)\rangle$.

For the single-valued flame front, all three flame edges are identical. In the case of multi-valued edges, the leading edge propagates into the reactants before the locally averaged flame front. In contrast, the trailing edge propagates into the reactants after the locally averaged flame front (see inset of figure S5b). The x-averaged edge lies in between the other two and has the effect of smoothing out artificial abrupt variations that may arise in the other two flame edges due to multi-valued folds. Our analysis of inner intermittency in the main text uses the leading flame edge definition specified in (S2.3). In addition, we have also used the definition of the locally averaged flame edge defined in (S2.2) in Appendix A to show that the anomalous scaling exponent remains unchanged when definition (S2.2) is used for the intermittency analysis instead of (S2.3). Appendix A also includes an additional test which further confirms that anomalous scaling and the inner intermittency it evidences are not an artifact of the representation of multi-valued wrinkles but a genuine feature of the flame dynamics.

S3. Properties of the turbulent flow field and the flame

The instantaneous flow field $\boldsymbol{u}(\boldsymbol{x},t)$ is obtained from the PIV measurements. The mean $\langle\boldsymbol{u}\rangle$ and fluctuating $\boldsymbol{u}'$ components of the velocity field are defined as

$$\boldsymbol{u}(\boldsymbol{x},t) = \langle\boldsymbol{u}(\boldsymbol{x})\rangle + \boldsymbol{u}'(\boldsymbol{x},t), \tag{S3.1}$$

where, $\langle\cdot\rangle$ denotes an average over time, so that $\langle\boldsymbol{u}(\boldsymbol{x})\rangle = 1/T\int_T \boldsymbol{u}(\boldsymbol{x},t)dt$. The averaging time $T(\geqslant 250\tau_\ell)$ is several times greater than the integral time τ_ℓ of the flow. The turbulent intensity is measured as: $\upsilon = \langle 1/3(\boldsymbol{u}'\cdot\boldsymbol{u}')\rangle$. Further, we define the velocity auto-correlation function as:

$$R(\boldsymbol{r}) = \langle\boldsymbol{u}'(\boldsymbol{x}\ \ \boldsymbol{r})\boldsymbol{u}'(\boldsymbol{x})\rangle. \tag{S3.2}$$

The longitudinal $f(r)$ and lateral $g(r)$ velocity correlation functions, normalized by the kinetic energy, are defined as

$$f(r) = \langle u_i(\boldsymbol{x}+r\hat{\boldsymbol{e}}_i)u_i(\boldsymbol{x})\rangle\,/u^2, \tag{S3.3}$$

$$g(r) = \left\langle u_j(\boldsymbol{x}+r\hat{\boldsymbol{e}}_i)u_j(\boldsymbol{x})\right\rangle/u^2. \tag{S3.4}$$

where, $\hat{e}_i$ indicates a unit normal along the index i.

The longitudinal and lateral correlation functions for the two flame configurations F1 and F2, measured using data from the boxed region in figure S6, are presented in figure

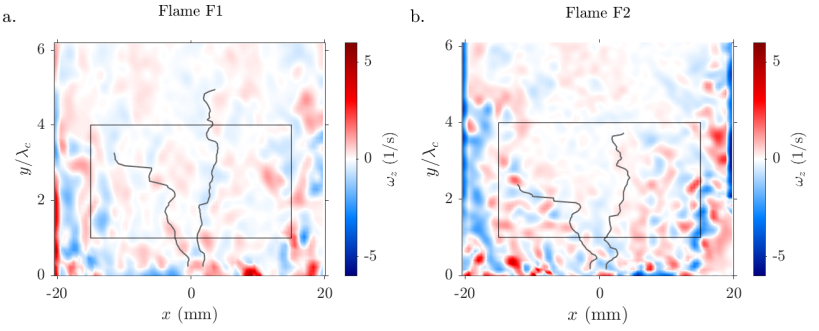

Figure S6: Depiction of the instantaneous flow-field for the two flame configurations considered in this study. The boxed region indicates the local region chosen for measuring velocity statistics for the experimental cases discussed here.

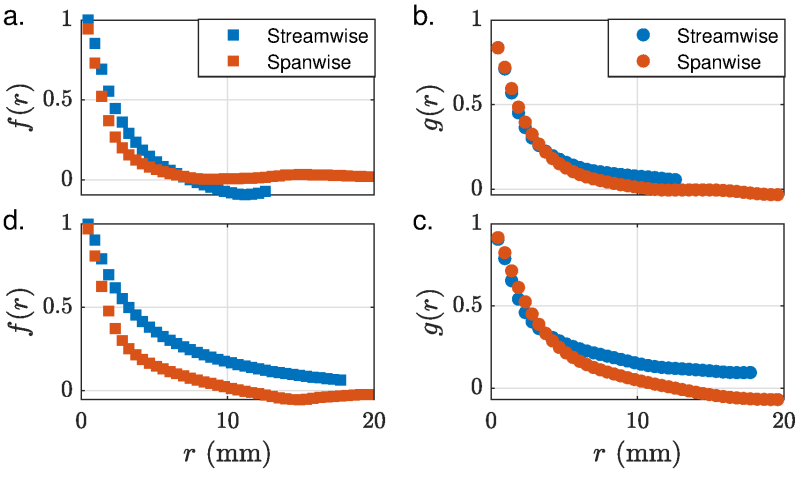

Figure S7: Longitudinal (f) and lateral (g) velocity correlation as a function of r (in mm) for flame configuration F1 (a,b) and F2 (c,d). The blue marker indicates measurement along the streamwise y-direction while the red marker indicates the measurement in the spanwise x-directions.

S7. Here, the blue (red) markers correspond to the correlation function measured along the streamwise (spanwise) direction. We note that for both F1 (panel a, b) and F2 (panels c,d) the correlations measured in the two directions are quite similar. Moreover, the velocity cross-correlations $\langle u'_x u'_y \rangle$, shown in figure S8 for the two flames, have relatively small values ($-0.2 < \langle u'_x u'_y \rangle < 0.1$) for $-15 < x < 15$ mm and $\lambda_c < y < 4\lambda_c$ (the boxed region in figure S6). These measurements indicate that the turbulent flow is close to isotropic within the local region in which we analyze the flame fluctuations.

The longitudinal correlations functions allow us to determine the integral and dissipative length scales of the flow. First, the integral length scale ℓ is determined as

$$\ell = \int_0^\infty f(r) dr. \tag{S3.5}$$

The integral scale Reynolds number is then determined as

$$Re_\ell = \frac{\rho u' \ell}{\mu}, \tag{S3.6}$$

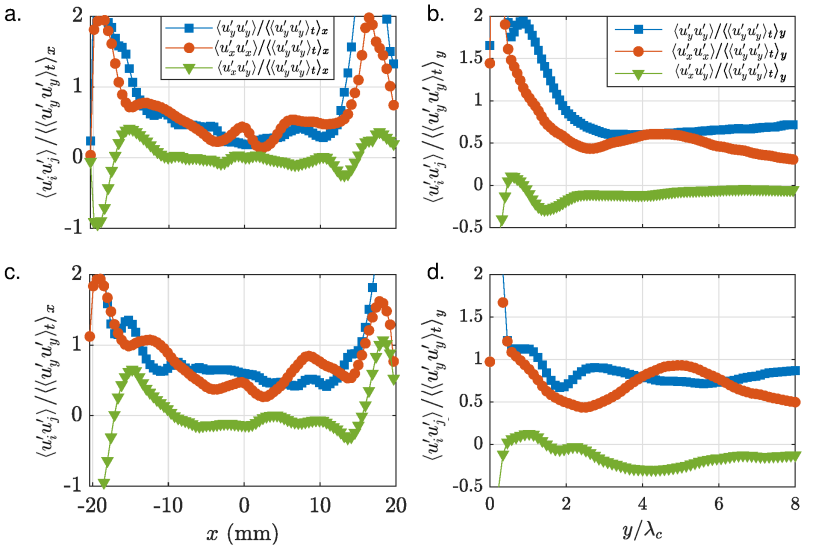

Figure S8: Time-averaged distribution of velocity cross-correlation as a function of (a,c) spanwise direction x measured at $y = 2\lambda_c$ and (b, d) streamwise direction y/λ_c at $x = -5$ mm for flame F1 (a, b) and F2 (c, d). The cross-correlation $\langle u'_x u'_y\rangle$ almost vanishes inside the boxed region indicated in figure S6.

where, the properties of the binary CH_4/air mixture ρ and μ are obtained following (Wilke 1950).

Next, the rate of turbulent kinetic energy dissipation is obtained from the large-scales as: $\varepsilon \sim \upsilon^3/\ell$. This finally allows us to determine the dissipative, Kolmogorov length η and time τ_η scales in terms of the integral scale quantities:

$$\eta/\ell = Re_\ell^{-3/4}, \qquad \tau\upsilon/\ell = Re_\ell^{-1/2}. \tag{S3.7}$$

To determine the key length and time scales of the flame, we begin by calculating the laminar flame speed s_L via Chemkin PREMIX calculations (Kee *et al.* 2011), using detailed chemistry simulated through GRIMech 3.0 mechanism (Smith *et al.* 1999) at 300 K and 1 bar. The flame thickness is calculated using the temperature gradient between the unburned reactants and burnt products, to wit,

$$\delta_F = \frac{T^u - T^b}{\max(dT/dx)}. \tag{S3.8}$$

The non-dimensional Damkohler (Da) and Karlovitz (Ka) numbers are then determined as

$$Da = \tau/\tau_{\text{chem}} = (\eta/\delta_F)^2, \qquad Ka = 1/Da. \tag{S3.9}$$

The Damköhler number of flame F1 is $Da = 3.91$ and F2 is $Da = 5.39$, and correspond to the boundary of corrugated flamelets and thin reaction zone (see figure S4).

The important flame length scales are the Gibson length scale (ℓ_g) and the Corrsin length scale (η_c). These are defined as

$$\ell_g = (s_L/\upsilon)^3\,\ell, \qquad \eta_c = (\mathcal{D}_M^3/\varepsilon)^{1/4} = Sc^{-3/4}\eta. \tag{S3.10}$$

Here, $\mathcal{D}_M$ is the Markstein diffusion. In determining the Corrsin scale η_c, we have taken the Schmidt number $Sc = \nu/\mathcal{D}_M = 0.7$ for both flame configurations following Tamadonfar &

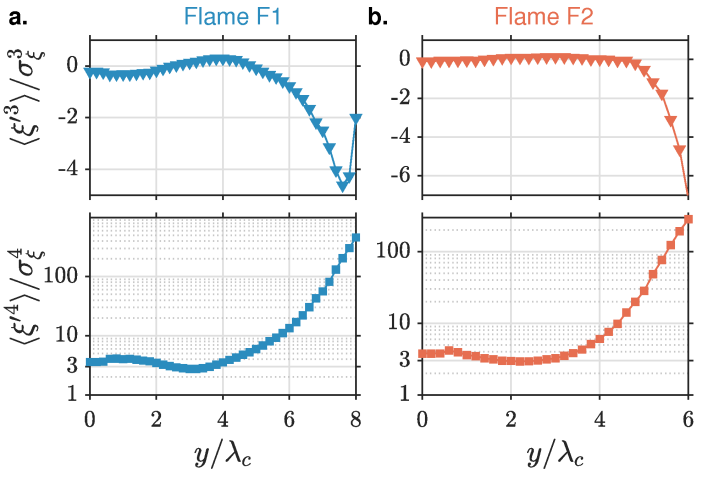

Figure S9: Variation of the skewness $\langle \xi'^3 \rangle / \sigma_\xi^3$ (top) and kurtosis $\langle \xi'^4 \rangle / \sigma_\xi^4$ (bottom) of flame fluctuations ξ' as a function of downstream location from flame holder y/λ_c for Flames F1 and F2.

Gülder (2014). The properties of the two turbulent flames configurations have been tabulated in Table 1 in the main manuscript.

S4. Outer intermittency in large-scale flame fluctuations

In figure 1(c,d) in the manuscript, we observed that the flame fluctuations, at large distances from the flame holder, depict an "on-off" type intermittent flapping behavior. To characterize this further, we plot the skewness and kurtosis of flame fluctuations as a function of y/λ_c for the two flames in figure S9. We can observe that while the kurtosis $K \approx 3$ and the skewness $Sk \approx 0$ for small distances ($0 \leqslant y \leqslant 4$), both properties depart dramatically from these Gaussian values as we move away from the flame holder. The large kurtosis implies the outer-intermittency of the large-scale flame motion, discussed in the main text. Note also that both flames depict negative skewness, implying that the large-scale flapping fluctuations are more likely to be in the direction of the unreacted fuel-air mixture than in the direction of the products.

S5. Scaling of power-spectrum and higher-order structure-function of Flame F2

The scaling of the power spectrum for flame F1 was depicted in figure 3 of the manuscript. The fluctuations associated with flame F2 also depict the same scaling behavior with a scaling exponent $\alpha \approx -2$ for measurements made between $1 \leqslant y/\lambda_c \leqslant 3$. This can be seen in figure S10. As was the case with F1, we observe that fluctuations measured at locations close to the flame holder depict a narrowband peak at the forcing frequency. However, for $y/\lambda_c > 1$, the effect of narrowband forcing gives way to a power-law scaling with $\alpha = -2$. The variation of α with y/λ_c is plotted, for both flames F1 and F2, in the inset in figure 2 of the main manuscript.

The compensated structure-function of the flame fluctuations for flame F2 is shown in figure S11. We notice that the structure functions depict well-defined scaling behavior where the scaling lasts for over one decade. The structure-functions are compensated by their scaling exponent ζ_p up to order $p = 6$. The variation of ζ_p with p, for both flames F1 and F2, has been shown in figure 4(a) of the main manuscript.

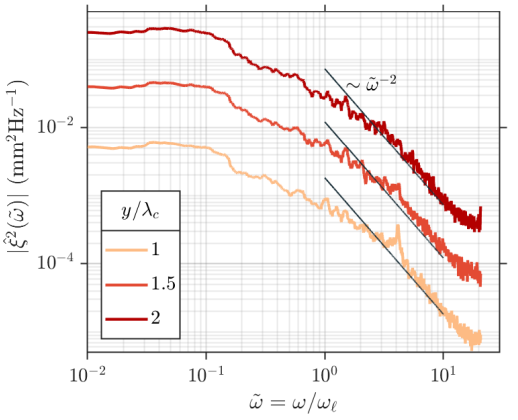

Figure S10: Temporal spectrum of flame fluctuations for Flame F2 measured at the indicated y/λ_c locations. For measurements at locations $y/\lambda_c < 1$, the flame response is harmonic with a peak at the forcing frequency $\tilde{\omega}_f$.

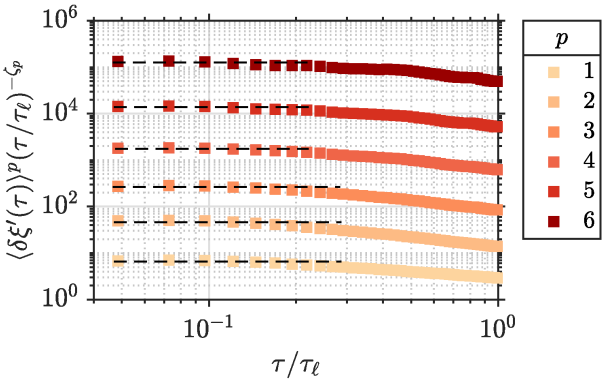

Figure S11: Structure function compensated by the estimated scaling $\tau^{-\zeta_p}$ for various order p as a function of the time delay τ for Flame F2.

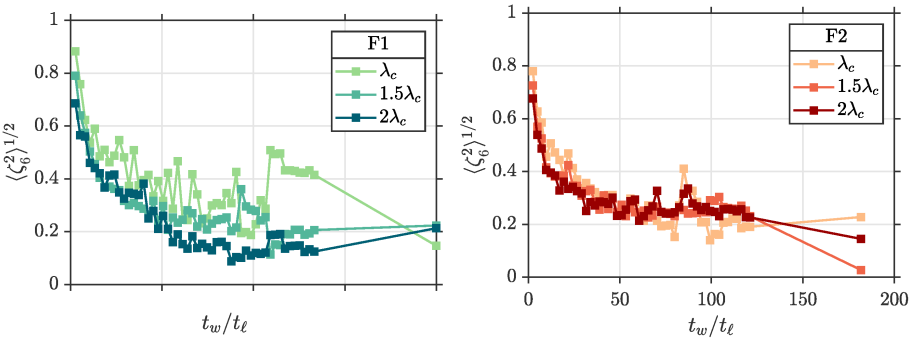

Figure S12: The variation in the standard deviation of ζ_p for $p = 6$ for various window sizes t_w at various y/λ_c locations for the two flames. We have chosen $t_w = 100t_\ell$ for obtaining the errorbars in figure 3a of the manuscript.

S6. Statistical uncertainty in the measurement of scaling exponents

In this section we describe how we estimated the error-bars associated with the scaling exponents ζ_p, shown in figure 4a in the main manuscript. For each flame configuration, the available data set consists of 21094 snapshots of the flame (at a sampling frequency $f_s = 1.25 \times 10^4$ Hz). Considering the azimuthal symmetry of the combustor setup, we calculated the flame fluctuations at a given y location from both the left and right flame edges, to obtain 42188 data points. This data set was then divided into subsets, each of which spanned a time window of size t_w. Each subset of data was then used to calculate the flame position increments, the structure functions and the scaling exponents. Thus, we obtain several values of ζ_p, one for each of the subsets of data. The mean of these values $\langle \zeta_p \rangle$ is reported as the measured values of the scaling exponent, while the standard deviation of these values $\langle \zeta_p^2 \rangle^{1/2}$ is used to estimate the associated statistical uncertainty.

To aid in selecting the size of the time window t_w, we calculate the standard deviation of the scaling exponents for various t_w. An illustrative example is depicted in figure S12, for the scaling exponent of the sixth-order structure-function. We see that for both flame F1 and F2, the standard deviation decreases as t_w is increased up to about $t_w = 80t_\ell$, beyond which the standard deviation saturates. So we choose $t_w = 100t_\ell$ as the time window and report the corresponding mean and standard deviation as the markers and error bars in figure 4a of the main manuscript.

REFERENCES

Chowdhury, B. R. & Cetegen, B. M. 2017 Experimental study of the effects of free stream turbulence on characteristics and flame structure of bluff-body stabilized conical lean premixed flames. *Combust. Flame* **178**, 311–328.

Humphrey, L. 2017 Ensemble-averaged dynamics of premixed, turbulent, harmonically excited flames. PhD thesis, Georgia Institute of Technology.

Humphrey, L. J., Emerson, B. & Lieuwen, T. C. 2018 Premixed turbulent flame speed in an oscillating disturbance field. *J. Fluid Mech.* **835**, 102–130.

Kee, R. J. & others 2011 Chemkin 10112, Reaction design: San Diego.

Kornilov, V. N., Schreel, K. R. A. M. & De Goey, L. P. H. 2007 Experimental assessment of the acoustic response of laminar premixed bunsen flames. *Proc. Combust. Inst.* **31** (1), 1239–1246.

LaVision 2006 Flowmaster PIV/PTV - systems. http://www.lavision.de/en/products/flowmaster/index.php.

Marshall, A., Venkateswaran, P., Noble, D., Seitzman, J. & Lieuwen, T. 2011 Development and characterization of a variable turbulence generation system. *Exp. Fluids* **51** (3), 611.

Otsu, N. 1979 A threshold selection method from gray-level histograms. *IEEE Trans. Sys. Man Cybern.* **9** (1), 62–66.

Petersen, R. E. & Emmons, H. W. 1961 Stability of laminar flames. *Phys. Fluids* **4** (4), 456–464.

Smith, G. P. & others 1999 Gri-mech 3.0 chemical mechanism.

Tamadonfar, P. & Gülder, Ö. L. 2014 Flame brush characteristics and burning velocities of premixed turbulent methane/air bunsen flames. *Combust. Flame* **161** (12), 3154–3165.

Truffaut, J. M. & Searby, G. 1999 Experimental study of the darrieus-landau instability on an inverted-'v'flame, and measurement of the markstein number. *Combust. Sci. Tech.* **149** (1-6), 35–52.

Wilke, C. R. 1950 A viscosity equation for gas mixtures. *J. Chem. Phys.* **18** (4), 517–519.